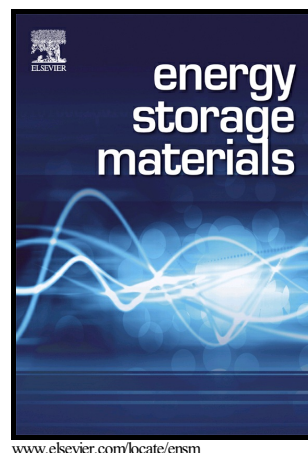


Hierarchical nanocarbon-MnO₂ electrodes for enhanced electrochemical capacitor performance

Hualei Qi, Zheng Bo, Shiling Yang, Liangping Duan, Huachao Yang, Jianhua Yan, Kefa Cen, Kostya (Ken) Ostrikov



PII: S2405-8297(18)30462-8
DOI: <https://doi.org/10.1016/j.ensm.2018.07.019>
Reference: ENSM459

To appear in: *Energy Storage Materials*

Received date: 17 April 2018
Revised date: 19 July 2018
Accepted date: 22 July 2018

Cite this article as: Hualei Qi, Zheng Bo, Shiling Yang, Liangping Duan, Huachao Yang, Jianhua Yan, Kefa Cen and Kostya (Ken) Ostrikov, Hierarchical nanocarbon-MnO₂ electrodes for enhanced electrochemical capacitor performance, *Energy Storage Materials*, <https://doi.org/10.1016/j.ensm.2018.07.019>

This is a PDF file of an unedited manuscript that has been accepted for publication. As a service to our customers we are providing this early version of the manuscript. The manuscript will undergo copyediting, typesetting, and review of the resulting galley proof before it is published in its final citable form. Please note that during the production process errors may be discovered which could affect the content, and all legal disclaimers that apply to the journal pertain.

Hierarchical nanocarbon-MnO₂ electrodes for enhanced electrochemical capacitor performance

Hualei Qi^a, Zheng Bo^a, Shiling Yang^a, Liangping Duan^a, Huachao Yang^a, Jianhua Yan^a, Kefa Cen^a, and Kostya (Ken) Ostrikov^{*, b, c, a}

^a State Key Laboratory of Clean Energy Utilization, Institute for Thermal Power Engineering, College of Energy Engineering, Zhejiang University, Hangzhou, Zhejiang Province, 310027, China. Email: bozh@zju.edu.cn

^b Institute for Future Environments and School of Chemistry, Physics and Mechanical Engineering, Queensland University of Technology, Brisbane, Queensland 4000, Australia. Email: kostya.ostrikov@qut.edu.au

^c CSIRO-QUT Joint Sustainable Processes and Devices Laboratory, P.O. Box 218, Lindfield, New South Wales 2070, Australia. Email: kostya.ostrikov@csiro.au

Acknowledgements

*Corresponding author at: Institute for Future Environments and School of Chemistry, Physics and Mechanical Engineering, Queensland University of Technology, Brisbane, Queensland 4000, Australia, Email: kostya.ostrikov@qut.edu.au

ACCEPTED MANUSCRIPT

This work was supported by the National Natural Science Foundation of China (No. 51722604) and Zhejiang Provincial Natural Science Foundation of China (No. LR17E060002). K. O. acknowledges partial support by the ARC.

Conflict of interest statement

Declarations of interest: none

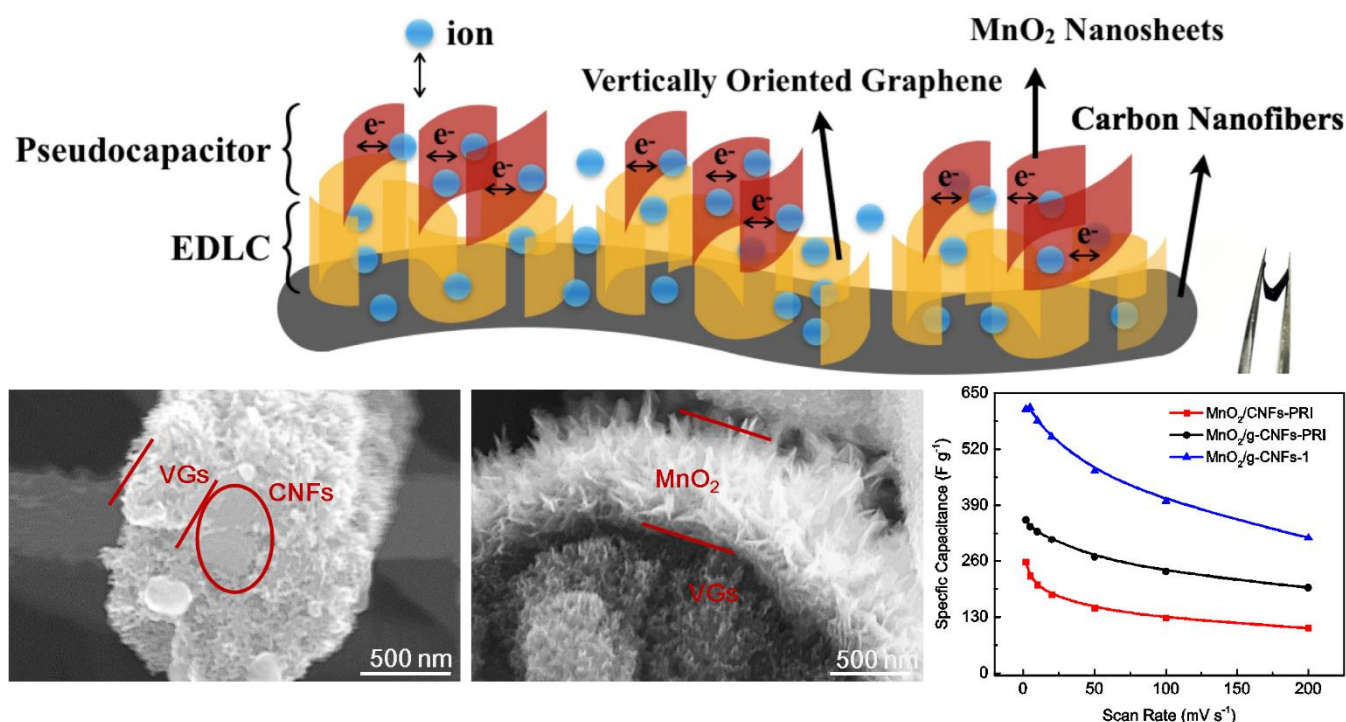
Abstract

High-capacity energy storage in electrochemical capacitors may benefit from the combination of electric double-layer capacitance (EDLC) and pseudocapacitance to lead to high specific energy and power beyond the current capacity of rechargeable batteries. However, commonly pursued combinations of non-conductive pseudocapacitive and conductive EDLC materials rarely achieve synergistic effects. This work addresses the issue by demonstrating unique hierarchical microstructured electrodes comprising uniformly dispersed MnO_2 nanoparticles on intentionally converted “pseudocapacitive” edges of plasma-grown Vertically Oriented Graphenes (VGs), with side-walls fully open to EDLC effects, and bonded at the base to the supporting highly conducting carbon nanofibers (CNFs), without any binder. The hierarchical structure combines the benefits of good conductivity of VGs and CNFs, the unique edge nucleation behavior and small size of MnO_2 nanoparticles, and the large surface areas of the exposed graphene walls. Moderate oxidation of VGs helps refine MnO_2 nanostructures and improve the cycle stability. The hybrid electrode delivers a specific capacitance of 612 F g^{-1} (32.7 F cm^{-3}) at scan rate of 2 mV s^{-1} and exhibits good stability 109% after 5000 CV cycles at the scan rate of 100 mV s^{-1} in three-electrode system. The asymmetric electrode configuration based on it reveals a specific energy of 30.4 Wh kg^{-1} (0.90 mWh cm^{-3}) and a specific power of 27.8 kW kg^{-1} (824 mW cm^{-3}) at 15 A g^{-1} . This work suggests new ways to produce hybrid MnO_2 -carbon hierarchical composite materials for the improved electrochemical capacitor performance.

Graphical abstract

ACCEPTED MANUSCRIPT

Combination of the pseudocapacitance of MnO_2 and EDLC of nanocarbon materials is realized by constructing a novel hierarchical structure of MnO_2 on edges of mildly oxidized VGs supported by CNFs, which forms thin and uniform MnO_2 nanosheets and exposed side walls of VGs. The hierarchical hybrid electrode exhibits high specific capacitance, good rate capability, excellent cycle stability, low resistance in three-electrode system. The associated asymmetric electrode system shows excellent values of the specific energy and specific power.



Keywords: vertically oriented graphenes; plasma nanofabrication; electric double-layer capacitance; pseudocapacitance; high specific energy

1. Introduction

Development of cheap, renewable, and sustainable energy sources is one of the most critical challenges of the century to respond to the fast consumption of oil, gas, and coal and the ever-escalating environmental problems. The efficient generation and use of energy is in high demand to enable the sustainable development of our society. Storage systems for intermittent renewable energy sources, such as solar and wind energy are attracting tremendous attention

from academic, commercial, and government sectors [1-3]. Electrochemical capacitors are among the most promising energy storage devices [4-6]. Common mechanisms of charge storage include electric double-layer capacitance (EDLC) and pseudocapacitance [7, 8]. The EDLC relies on conductive carbon-based electrode materials (e.g., activated carbon, graphene, carbon nanotubes, etc. [6, 9-13]) and physical adsorption/desorption of ions on the electrode surface. However, despite the high specific power, the specific energy achievable in EDLC electrochemical capacitors is not remarkable.

On the other hand, pseudocapacitor electrodes realize energy storage based on dual energy storage processes [3, 14, 15], the electric double layer capacitance at the surface and the redox reaction near the surface [16]. However, the common pseudocapacitor transition metal oxide materials [17-20] are almost non-conductive, which limits both the specific energy and specific power. Synergistic combination of the EDLC and pseudocapacitive effects is very promising to mitigate the limited conductivity of pseudocapacitive materials and increase the capacitance [21-25]. This can be achieved by stacking both kinds of materials to deliver maximum performance and enhancing rather than compromising the primary effects from each other. The high specific energy and power achieved in this way may lead to advanced electrochemical capacitor performance.

Fig. 1. Synergy of electrostatic double layer and pseudocapacitive effects realized by hierarchical stacking of MnO_2 on the edges of VGs supported by large-area, flexible carbon nanofibers. This way of stacking fully opens the side-walls of VGs to electrolyte ions and ensures maximum efficiency from both primary mechanisms of charge storage. High conductivity of VGs and CNFs and covalent bonding between them ensure high charge transfer rates leading to excellent specific energy and power of the nanostructured hierarchical hybrid electrochemical capacitor electrode.

This work reports on such a synergistic combination of materials arranged in hierarchical high-performance and stable micro-structured electrochemical capacitor electrodes. Compared with other reported MnO_2 -based hierarchical structures [26], the unique point of this work is the stack of Vertically Oriented Graphenes (for simplicity referred to as vertical graphenes, VGs), also called carbon nanosheets or carbon nanowalls (CNWs), which are grown directly [27], with very high density on the surface of inter-woven carbon nanofibers (CNFs). The VGs simultaneously enable two functions: the EDLC function by presenting open side-walls to electrolyte ions and supporting dense chains of small MnO_2 nanoparticles for pseudo-capacitive effect on their open top edges. The highly conducting VGs covalently bonded to the supporting CNFs provide conducting paths for the electric charges

transported through both the EDLC and pseudocapacitive interactions. The conceptual novelty, direct fabrication of the hierarchical structure and the charge storage mechanism are sketched in Fig. 1. This method is more simple and low-cost for building an open 3D composite for full contact with electrolyte than other deposition methods via co-dispersant, electrolytic KMnO_4 , and sacrificial coating template, etc. Electrophoretic deposition involving separately prepared MnO_2 , carbon-based materials, and a steady colloidal mixture of them by co-dispersant is a complex multi-stage process with limited cost-efficiency [28]. Moreover, MnO_2 deposits via electrolytic deposition of KMnO_4 often appear agglomerated particles in shape, difficult to contact with electrolytes [29]. Besides, due to the removal of the template, the sacrificial coating template method is also complicated, time-consuming and high-cost [26].

The key pseudocapacitive element MnO_2 is a naturally abundant, low-cost, non-toxic, and structurally versatile material featuring a high theoretical specific capacitance of 1370 F g^{-1} [26, 30-34]. However, intrinsically low conductivity (10^{-5} to $10^{-6} \text{ S cm}^{-1}$) [26, 35] of pure MnO_2 limits the transport of electrons and ions, leading to poor specific capacitance of 250 F g^{-1} [36-38]. Attempts to combine MnO_2 with carbon-based EDLC materials help improve the overall conductivity [30, 39-44], yet at the expense of the EDLC effect because MnO_2 nanoparticles in most cases occupy a large fraction of the surface area of EDLC materials thereby reducing the electrostatic double layer effects. This is why construction of hierarchical composite materials which simultaneously expose both nanocarbon and nanostructured MnO_2 materials and support the effective utilization of MnO_2 for maximizing their primary effects synergistically is on the agenda.

The VGs are among the most effective EDLC materials and are the key functional elements of our hierarchical structure. Their remarkable conductivity is used to carry electric charge, while micro-spaces between the vertical graphenes provide large surface area for EDLC and simultaneously prevent dense packing of MnO_2 nanoparticles [45, 46]. The dense, undulating, and high active edges on top of VGs can support nucleation of a very large number of small MnO_2 nanoparticles [47, 48]. Besides, VGs edges enhance the reactivity of active materials during charge/discharge processes [49-52], which we hypothesise should also work with effective utilization of MnO_2 pseudocapacitive materials.

The last but not the least structural element of the hierarchical structure is electrospun carbon nanofibers (CNFs) that support the VGs without any commonly used binders. The covalent bonds between VGs and CNFs in g-CNF structures are expected to ensure high electron transport rates [53, 54]. Besides, the porous and multilayer structure and good mechanical properties of CNFs [55-57] provide plentiful space for the growth of

ACCEPTED MANUSCRIPT

dense patterns of VGs and MnO₂ nanostructures, while simultaneously keeping the electrode from damage during the fabrication and tests processes [38, 58-63]. Moreover, the sizes and distribution of MnO₂ nanoparticles and hence the electrochemical performance of the hybrid electrode materials, were further improved by mild oxidation of g-CNFs structure. The designation and performance of the electrode structures produced in this work are summarized in Table 1.

2. Experimental

2.1. Preparation of CNFs films

Polyacrylonitrile (PAN, Mn = 150kDa) powder was dissolved in N, N-dimethylformamide (DMF) with a mass concentration of 10%. The mixture was kept stirred for 4 h at a temperature of 50 °C and then stood for 2 h to get a homogeneous solution. Apparatus used for electrospinning was homemade. Electrospinning processes were carried out at 26 ± 2 °C with humidity of $50 \pm 2\%$. DC voltage applied between the needle and collector was fixed at 14.5 kV, distance between them as 15 cm. The flow rate was kept at approximately 1.5 mL h⁻¹. Films were deposited on a rotary drum of stainless steel with a diameter of 10 centimeters covered by an aluminum foil. The as-obtained films were then removed to an air blowing thermostatic oven to get rid of the residual solvent for 48 h at 50 °C. Consequently, they got into pre-calcination process carried out for 5 h at 280 °C in air with a heating rate of 1 °C min⁻¹. The films were further carbonized in a tube furnace under a flowing Ar atmosphere (75 standard cubic centimeters per min) for 1 h at 1000 °C with a heating rate of 1 °C min⁻¹. Finally, they were cooled to 30 °C still under Ar ambience with a cooling rate of 1 °C min⁻¹.

2.2. Preparation of g-CNFs films

G-CNFs films were fabricated with a homemade microwave plasma enhanced CVD (MPECVD) system. A bias of 50 V was applied to CNFs and the pressure was maintained at 600 Pa during the growth process. Before the generation of carbon plasma, the system was heated to 600 °C by a H₂ microwave of 350 W. CH₄ (10 sccm, flow rate H₂:CH₄ = 5:1) was used as the carbon source. After a 2-min growth, the microwave power was shut down and the sample was cooled down to room temperature under the protection of H₂.

2.3. Electrodeposition of MnO_2 on g-CNFs films

MnO_2 was electrodeposited on substrates in a three-electrode configuration using a simple pulse galvanostatic method at room temperature. Pristine CNFs or g-CNFs films ($1 \times 1 \text{ cm}^2$, CNFs-PRI and g-CNFs-PRI) were used as the working electrode, platinum plate electrode ($2 \times 2 \text{ cm}^2$) was used as the reference/counter electrode, and saturated calomel electrode (SCE) was used as the reference electrode. A neutral electrodeposition solution was prepared by mixing of 0.1 M manganese acetate tetrahydrate ($\text{Mn}(\text{Ac})_2 \cdot 4\text{H}_2\text{O}$), 0.1 M anhydrous sodium sulfate (Na_2SO_4), 0.1 M ammonium acetate (NH_4Ac), and 0.05 g L^{-1} sodium laurylsulfonate. A pulsed current of 5 mA was applied to electrodes with the on and off time set as 2 and 1s in one pulse. MnO_2 was obtained after 2250 pulses. Electrodepositions were performed using Autolab electrochemical workstation (PGSTAT302N) controlled by NOVA software. The composites were then washed in deionized water and placed in a vacuum drying oven for 24 hours at 60°C . The loading mass of MnO_2 was calculated from the weight difference before and after the electrodeposition using a microbalance. Composites of MnO_2 on oxidized CNFs or g-CNFs substrates were further researched. CNFs-PRI or g-CNFs-PRI substrates were immersed into a mixed acid of concentrated sulfuric acid (H_2SO_4) and nitric acid (HNO_3) (volume ratio 3:1) for 1, 3, and 5 mins (CNFs-1, g-CNFs-1, g-CNFs-3, and g-CNFs-5) and then washed in deionized water for several times. Before the electrodeposition, they were dried at 60°C overnight. The mass loading of MnO_2 on CNFs-PRI, g-CNFs-PRI, CNFs-1, g-CNFs-1, g-CNFs-3, g-CNFs-5 are 120, 110, 100, 80, 140, and $140 \mu\text{g cm}^{-2}$, respectively, labeled as $\text{MnO}_2/\text{CNFs-PRI}$, $\text{MnO}_2/\text{g-CNFs-PRI}$, $\text{MnO}_2/\text{CNFs-1}$, $\text{MnO}_2/\text{g-CNFs-1}$, $\text{MnO}_2/\text{g-CNFs-3}$, and $\text{MnO}_2/\text{g-CNFs-5}$. The weight fractions of electrodeposited MnO_2 on CNFs-PRI, g-CNFs-PRI, CNFs-1, g-CNFs-1, g-CNFs-3, g-CNFs-5 are 16.7%, 15.5%, 14.3%, 11.8%, 18.9%, and 18.9%, respectively, which are comparable with previous report [64].

2.4 Materials characterization

Microstructure information and chemical compositions of the composites were characterized by a LabRAM HR Evolution laser Raman spectroscopy (532nm, Horiba Jobin Yvon) and X-ray photoelectron spectroscopy (XPS, VG Escalab Mark II) with a monochromatic Mg $\text{K}\alpha$ X-ray source (1253.6 eV, West Sussex). The morphologies of the samples were observed by a high-resolution field-emission scanning electron microscope (SEM, Hitachi SU-70) and a transmission electron microscope (TEM, JEOL JEM-2100).

2.5 Electrochemical measurement

The composite electrodes were tested in a three-electrode system as the work electrode, platinum plate electrode as the reference/counter electrode, and saturated calomel electrode (SCE) as the reference electrode. Carbon nanofiber membrane served as the current collector [54]. The system was tested using cyclic voltammetry (CV) and galvanostatic charge/discharge (GCD) with potential ranging from 0 to 0.8 V at different scan rates. The electrolyte was a hybrid aqueous solution of 1 M Na₂SO₄ and 0.03 M disodium hydrogen phosphate dodecahydrate (Na₂HPO₄·12H₂O) at room temperature. Na₂HPO₄·12H₂O has a capability of maintaining steady electrochemical reaction which is useful for exploiting the best electrochemical performance of the electrodes in this work [65]. Electrochemical impedance spectra (EIS) were measured with a 5 mV AC signal over the frequency ranging from 0.01 Hz to 100 kHz. Cyclic stability tests over 5000 cycles were carried out by CV (0-0.8 V) at a scan rate of 100 mV s⁻¹.

The gravimetric and areal specific capacitance (C_M and C_A) based on CV curves of the three-electrode system are determined by [59, 66],

$$C_M = \frac{1}{2sM\Delta V} \int I dv \quad (1)$$

$$C_A = \frac{1}{2sA\Delta V} \int I dv \quad (2)$$

$$C_V = \frac{1}{2sV\Delta V} \int I dv \quad (3)$$

where C_M (F g⁻¹), C_A (mF cm⁻²), and C_V (F cm⁻³) are the gravimetric, areal, and volumetric specific capacitance, respectively, s is the scan rate (V s⁻¹), M is the mass of the active electrode material (g), A is the geometrical area of the electrode (cm²), V is the volume of the electrode (cm³), ΔV is the potential window for charge, I is the instantaneous current on CV curves, and v is the applied voltage.

The calculation of C_M based on GCD curves is carried according to the following equation [67],

$$C_M = \frac{I \Delta t}{\Delta V} \quad (4)$$

where I is the discharge current density (A g⁻¹), Δt is the discharge time, and ΔV is the potential window after potential drop.

An asymmetric electrochemical capacitor was prepared to explore the practical application of the composite material. In order to directly contrast with previous related reports which mostly used single-electrolyte solution of 1 M Na₂SO₄, 1 M Na₂SO₄ was used as the electrolyte without Na₂HPO₄·12H₂O added in. The asymmetric

electrode system consisted of the hierarchical material as the positive electrode and g-CNFs-PRI as negative electrode (AMG). The two electrodes with different materials possess different gravimetric specific capacitances (C_M^+ and C_M^-), which is the reason for the charge balance ($q^+ = q^-$) can be used for mass matching[68, 69],

$$M^+ C_M^+ E^+ = M^- C_M^- E^- \quad (5)$$

where M is the mass of active material of one electrode, C_M^+ and C_M^- are calculated from CV tests at the scan rate of 10 mV s^{-1} in three-electrode system, and E is the corresponding potential limit. Each electrode was linked with external Autolab through a platinum wire. For different potential limits (from 0.8 to 2.0 V), AMG was tested by CV at a scan rate of 10 mV s^{-1} and GCD at scan rate of 1 A g^{-1} . For the potential limit of 2.0 V, AMG was tested by CV at scan rates from 5 to 200 mV s^{-1} and GCD curves at scan rates from 1 to 15 A g^{-1} .

The specific energy E (Wh kg^{-1}) and the specific power P (kW kg^{-1}) based on GCD curves of AMG are calculated using equations (6) and (7) [67],

$$E = 0.5 \frac{C_M \Delta U^2}{3.6} \quad (6)$$

$$P = 3.6 \frac{E}{\Delta t} \quad (7)$$

where Δt is the discharge time and ΔU is the potential window.

3. Results and discussion

3.1. Morphology and structure characterization of composite electrodes

Fig. 2. Microstructure of the hierarchical hybrid electrodes imaged by FE-SEM shows the possibility to arrange MnO_2 nanosheets on top of the VGs edges, while the VGs are supported by carbon nanofibers. FE-SEM images of (a) CNFs, (b) g-CNFs, (c) Cross section of g-CNFs, (d) $\text{MnO}_2/\text{CNFs-PRI}$, (e) $\text{MnO}_2/\text{g-CNFs-PRI}$, and (f) Cross section of $\text{MnO}_2/\text{g-CNFs-PRI}$. Notation of samples is explained in Table 1.

The surface morphologies of CNFs-PRI, g-CNFs-PRI, $\text{MnO}_2/\text{g-CNFs-PRI}$, and $\text{MnO}_2/\text{CNFs-PRI}$ were imaged by SEM microscopy. The average diameter of CNFs-PRI in Fig. 2a is estimated to be 315 nm with a standard deviation (SD) of 18 nm through 50-100 random places using ImageJ2x software (National Institute of Health, MD, USA). It increases to $1.48 \mu\text{m}$ (SD = 140 nm) after the successful growth of VGs in Fig. 2b. The cross section of g-CNFs-PRI in Fig. 2c exhibits a two-phase structure, cauliflower-like VGs around the fiber

and flat CNF at the center. The observed smooth interphase between VGs and CNFs manifests the existence of covalent binding. $\text{MnO}_2/\text{CNFs-PRI}$ and $\text{MnO}_2/\text{g-CNFs-PRI}$ samples in Fig. 2d-e possess average diameters of 1.56 (SD = 210 nm) and 2.73 (SD = 170 nm) μm for fibers with deposits, respectively, proving the successful building of the hierarchical structures. Both exposed dark VGs (at the bottom) and light MnO_2 (on the surface) observed in the red rectangles (Fig. 2e) show that both EDLC and pseudocapacitance responses are possible. Despite the similar shape of MnO_2 nanosheets on both substrates, they are thinner (25.6 nm) on g-CNFs-PRI and more homogeneous (SD = 7.60 nm) than those on CNFs-PRI (35.7 nm, SD = 9.59 nm), seen from the insets in Fig. 2d-e and Fig. S1, attributed to the long, undulating, and high active edges of VGs favoring grain refining. However, a clear phase boundary between MnO_2 and VGs appears on the cross section of $\text{MnO}_2/\text{g-CNFs-PRI}$ in Fig. 2f, directly evidencing the nucleation of MnO_2 on edges of VGs.

The surface layer under 10 nm of CNFs-PRI between the red parallel lines in Fig. 3a, indicates the fibers were only mildly graphitized, while the inside remained amorphous. However, the high temperature and reductive hydrogen atmosphere during MPECVD modify CNFs (e.g., reduce and produce defects), as seen from the red ellipse in TEM image of Fig. 3b. This offers an opportunity for VGs with dense edges to grow all over the large surface areas of the fibers, seen from the magnified TEM image of Fig. 3b. TEM image in Fig. 3c shows that VGs grow on surface of CNFs vertically. The high-resolution TEM (HRTEM) images shown in Fig. 3d-e were obtained to further investigate the structure of VGs. Nanosheets of 3-9 layers with inter-planar spacing of 0.34 nm and regularly distributed carbon can be observed in the HRTEM micrographs, consistent with the previous reports confirming regular graphitic structure of VGs [45, 46]. Both the graphene walls and the internal graphitization could improve the CNFs conductivity.

Fig. 3. Transmission electron microscopy showing dense patterns of VGs seamlessly incorporated into the supporting carbon nanofiber structure. TEM and magnified TEM images of (a) CNFs-PRI and (b) g-CNFs-PRI samples; TEM (c) and HRTEM (d-e) images of VGs; locations 1, 2, and 3 in (d) show VGs sheets with 3, 6, and 9 layers; (f) Raman spectra of the various electrode materials; (g) High resolution Raman spectrum of $\text{MnO}_2/\text{g-CNFs-PRI}$ sample.

Variations of fiber microstructure were further characterized by Raman spectroscopy, shown in Fig. 3f. D defect band (1350 cm^{-1}) is induced by sp^3 -hybridized carbon, whereas G band (1585 cm^{-1}) is related to the in-plane stretching vibration of sp^2 -hybridized carbon atom.[70] Therefore, the intensity ratio of D band to G band

(I_D/I_G ratio) represents the defect level of graphene-based materials. The I_D/I_G ratio of CNFs-PRI (1.01) is much lower than that of g-CNFs-PRI (2.38). Their half-peak width, however, is several times larger owing to the low graphitization degree. The high defect level for g-CNFs-PRI is due to the huge defects on edges and numerous regions separated by the gaps between graphenes. The bands at about 600 cm^{-1} appearing in Raman spectra of $\text{MnO}_2/\text{CNFs-PRI}$ and $\text{MnO}_2/\text{g-CNFs-PRI}$ belong to MnO_2 . The enlarged MnO_2 band of $\text{MnO}_2/\text{g-CNFs-PRI}$ in Fig. 3g consists of two peaks (586 cm^{-1} and 628 cm^{-1}), attributed to stretching vibration of the Mn-O bond on the base and in the vertical plane of $[\text{MnO}_6]$ octahedron [71], respectively (Enlarged MnO_2 band of $\text{MnO}_2/\text{CNFs-PRI}$ is in Fig. S2). Therefore, we surmise the manganese oxide is MnO_2 .

Fig. 4. XPS analysis reveals dominant carbon-carbon and Mn-oxygen bonds which are beneficial for both structural stability and dual charge storage mechanism. (a) XPS spectra of various electrode materials; De-convoluted XPS C 1s spectra of (b) CNFs-PRI and (c) g-CNFs-PRI; (d) XPS Mn 2p, (e) Mn 3s, and (f) De-convoluted O 1S spectrum of $\text{MnO}_2/\text{g-CNFs-PRI}$.

Variation in chemical compositions of the electrode materials and confirmation of the oxidation state of manganese were investigated by XPS characterizations. The C/O ratio of g-CNFs-PRI (17.17) is much greater than that of CNFs-PRI (2.59), based on the spectra in Fig. 4a, suggesting the deposition of nanocarbon on the CNF-PRI during the MPECVD process. The C 1s spectra of CNFs-PRI and g-CNFs-PRI are de-convoluted with four components which are C=C bond (284.3 eV), C-C bond (285.4 eV), C-O bond (286.5 eV), C=O bond (287.6 eV), and O-C=O bond (289.1 eV), as shown in Fig. 4b-c [72, 73]. The 18% higher content of C=C and C-C bonds (83.7%) than CNFs-PRI and the hardly noticeable O-C=O bond in g-CNFs-PRI were induced by the carbon deposition during MPECVD process. However, the content of C-C bond has a larger increase than C=C bond, suggesting more defects like carbon dangling bond existing on edges of g-CNFs-PRI.

MnO_2 deposits diminished C 1s peak, enhanced O 1s peak, and introduced Mn 3s and Mn 2p peaks in XPS spectra of the composites. Mn 3s and O 1s core level spectra can be used to assess the oxidation state of manganese [33, 71]. Fig. 4d shows the Mn 2p peaks with an energy separation of 11.7 eV between $2p_{1/2}$ (653.6 eV) and $2p_{3/2}$ (641.9 eV), in accordance with the results reported in literature [31], suggesting a manganese valence of 4. Since the electrons in 3s and 3d orbitals produce parallel spin coupling during the photoelectron ejection, a pair of split peaks appear for Mn 3s core level spectrum [71]. The lower peak separation during the photoelectron emission means fewer electrons in 3d orbital,

implying higher manganese valence. Consequently, the low peak separation of 4.8 eV with signals appearing at 83.5 and 88.3 eV of the Mn 3s multiplet in Fig. 4e gives another proof about the dominant Mn^{4+} state [71]. The O 1s core level spectrum was de-convoluted into three components, including Mn-O-Mn bond (529.8 eV) for tetravalent oxide, Mn-O-H bond (532.0 eV) for a hydrated trivalent oxide, and H-O-H bond (533.1 eV) for residual structure water, as shown in Fig. 4f [74]. The contents of MnO_2 and MnOOH in $\text{MnO}_2/\text{g-CNFs-PRI}$ are 67.8% and 11.8%, respectively, equivalent to According to the de-convoluted O 1s spectra and the valence calculation equation (Fig. S2), the oxidation state of MnO_2 on CNFs-PRI and g-CNFs-PRI are 3.79 and 3.83, respectively [33, 64], slightly lower than 4, indicating partial Mn^{3+} ions were not able to be oxidized to be Mn^{4+} . The surface vacancy of MnO_2 is responsible for existence of Mn^{3+} , which is difficult to be avoided due to the inherent crystal defect. The valences close to 4 demonstrate the Mn^{4+} is dominant in the oxide. Therefore, “ MnO_2 ” is used to describe all the manganese oxides involved in this article despite some deviation from the stoichiometric value.

3.3. Electrochemical performance of the composite electrodes

Fig. 5a shows CV curves for $\text{MnO}_2/\text{g-CNFs-PRI}$ at scan rates from 2 to 200 mV s^{-1} with potential ranging from 0 to 0.8 V in a three-electrode system (CV curves for $\text{MnO}_2/\text{CNFs-PRI}$ are in Fig. S3). They reach much higher current densities than those of $\text{MnO}_2/\text{CNFs-PRI}$, as shown in Fig. 5b-c. This superiority indicates that, due to the good conductivity of VGs and the thinner and more homogenous 3D MnO_2 nanosheets on edges, $\text{MnO}_2/\text{g-CNFs-PRI}$ electrode supports more efficient electron transport, shorter ion diffusion routes, and presents huge surface areas for ion adsorption even at high scan rates. Therefore, compared with CNFs-PRI, g-CNFs-PRI is better suited for formation of hierarchical nanocarbon- MnO_2 structure.

Fig. 5. Substantial improvement of electrochemical performance by stacking of MnO_2 nanosheets on top of VG edges in a three-electrode system. (a) The whole CV curves for $\text{MnO}_2/\text{g-CNFs-PRI}$; (b-c) CV curve comparisons for $\text{MnO}_2/\text{CNFs-PRI}$ and $\text{MnO}_2/\text{g-CNFs-PRI}$ at different scan rates; (d-e) C_M and C_A values vs. scan rate for various electrode materials; (f) Capacitance retention for $\text{MnO}_2/\text{CNFs-PRI}$ and $\text{MnO}_2/\text{g-CNFs-PRI}$ after a cycle stability test.

As shown in Fig. 5d, the overall C_M value of CNFs-PRI based on the mass of CNFs-PRI is lower than 2 F g^{-1} . As for g-CNFs-PRI, C_M value based on the mass of both VGs and CNFs-PRI, is almost four times as high as

that of CNFs-PRI, indicating the significant EDLC effect of VGs with tiny mass. The C_M value of $\text{MnO}_2/\text{g-CNFs-PRI}$ at scan rate of 2 mV s^{-1} is 356 F g^{-1} , higher than the reported 250 F g^{-1} for pure MnO_2 [36-38]. The rate capability of $\text{MnO}_2/\text{g-CNFs-PRI}$ at high scan rate of 200 mV s^{-1} (198 F g^{-1}) is 55.6%. In contrast, it decreases by 59.5% for $\text{MnO}_2/\text{CNFs-PRI}$ from 257 F g^{-1} at 2 mV s^{-1} to 104 F g^{-1} at 200 mV s^{-1} . The C_A and C_V values of CNFs-PRI and g-CNFs-PRI in Fig. 5e and Fig. S3 further show the capacity difference in the case of the same electrode area and volume. After subtracting the contribution of supports, the pure MnO_2 on CNFs-PRI and g-CNFs-PRI delivers specific capacitances of 250 and 329 F g^{-1} (97% and 92% of the total amount), respectively, which stresses the advantage of combining EDLC from VGs and pseudocapacitance from MnO_2 . The reaction associated with double-layer capacitance and pseudocapacitance of manganese dioxide can be expressed as,



where N^+ represents electrolyte cations (H^+ and Na^+ in this work). Physical adsorption/desorption of N^+ at the surface of MnO_2 and interaction/extraction of N^+ near the surface follow the mechanism of dual energy storage processes. It is widely believed repeated interaction/extraction of N^+ could cause dissolution of manganese and irreversible structure failure, which is unfavorable for cycle stability [75, 76]. After 5000 CV cycles at scan rate of 100 mV s^{-1} , shown in Fig. 5f, the capacitance retentions for $\text{MnO}_2/\text{g-CNFs-PRI}$ and $\text{MnO}_2/\text{CNFs-PRI}$ electrodes are 93% and 88%, respectively. It is worth noting that the hierarchical structure of the electrodes are maintained and MnO_2 nanosheets are still anchored firmly on the surface of the supports, resulting in good mechanical strength and flexibility, shown in Fig. S4.

GCD curves in three-electrode system for $\text{MnO}_2/\text{g-CNFs-PRI}$ at current densities from 2 to 50 A g^{-1} in Fig. 6a span longer charge/discharge time than those for $\text{MnO}_2/\text{CNFs-PRI}$ (Fig. S5). The C_M values of $\text{MnO}_2/\text{g-CNFs-PRI}$ is 441 F g^{-1} at scan rate of 5 A g^{-1} , over 59% higher than the 252 F g^{-1} of $\text{MnO}_2/\text{CNFs-PRI}$ (Fig. S6). This further highlights the strength of the exposed VGs and refined MnO_2 nanosheets for enhanced both EDLC and pseudocapacitance.

Fig. 6. Hybrid hierarchical electrodes show good high-frequency response in a three-electrode system. (a) The whole GCD curves for $\text{MnO}_2/\text{g-CNFs-PRI}$; (b) Nyquist plots (line represents fitting data, and scatter raw data) and equivalent circuit in the inset, and (c) the real and imaginary parts of capacitance vs. frequency for $\text{MnO}_2/\text{g-CNFs-PRI}$ and $\text{MnO}_2/\text{CNFs-PRI}$ samples.

The Nyquist impedance spectra of the two materials by EIS tests were fitted by ZSimpWin with chiSq values controlled under 10^{-4} , shown in Fig. 6b [77, 78]. Intercept on real axis at high frequencies represents the internal resistance (R_s) of electrode and electrolyte. It is 9.2Ω for $\text{MnO}_2/\text{CNFs-PRI}$ and reduces to 5.6Ω for $\text{MnO}_2/\text{g-CNFs-PRI}$, reflecting the positive effect of VGs. The subsequent depressed arc caused by the charge-transfer resistance (R_{ct}) at electrode interfaces is 7.1Ω for $\text{MnO}_2/\text{g-CNFs-PRI}$ electrode, lower than that of $\text{MnO}_2/\text{CNFs-PRI}$ (8.2Ω) according to the inset in Fig. 6b. These findings support the view that the edge-electrodeposition behavior of MnO_2 and the formed thinner nanosheets can attract more electrons at the surface, benefiting redox reactions. The straight lines inclined at a constant phase angle to the real axis (Warburg region) at intermediate frequencies are associated with the semi-infinite diffusion of cations in the electrode. The higher real values Z' of $\text{MnO}_2/\text{CNFs-PRI}$ electrode appear presumably because of a lower reactivity of the thick MnO_2 nanosheets on CNFs-PRI support [79]. The linear tail at low frequencies corresponds to the accumulation of cations at the impermeable interface through finite diffusion. The slightly larger tail slope of $\text{MnO}_2/\text{g-CNFs-PRI}$ represents a better capacitance performance.

The evolution of capacitance can also be displayed by the function of complex capacitance ($C(\omega)$) and frequency, which defined as [80]:

$$C(\omega) = C'(\omega) - jC''(\omega) \quad (9)$$

The relationship between the real and imaginary parts of the capacitance with the frequency are expressed as [80]:

$$C'(\omega) = \frac{-Z''(\omega)}{\omega|Z(\omega)|^2} \quad (10)$$

$$C''(\omega) = \frac{-Z'(\omega)}{\omega|Z(\omega)|^2} \quad (11)$$

where $\omega=2\pi f$, and f is frequency of current. The $C'(\omega)$ values of the two electrodes at frequency of 0.01 Hz in Fig. 6c are corresponding to the CV results. The characteristic relaxation time constant (CRTC) of $\text{MnO}_2/\text{g-CNFs-PRI}$ is 1.5 s, lower than that of $\text{MnO}_2/\text{CNFs-PRI}$ (5s), coinciding with the rate capability reflecting from the capacitance.

3.4. Effect of oxidation of substrates on the ternary composite electrodes

The superiority of $\text{MnO}_2/\text{g-CNFs-PRI}$ to $\text{MnO}_2/\text{CNFs-PRI}$ emphasizes the outstanding role of VGs in supporting MnO_2 . However, compared with previous work [81], the potential of the ternary $\text{MnO}_2/\text{g-CNFs}$ electrode was not fully exploited. Therefore, structural optimization was needed. Considering the high reactivity of edges and the electrodeposition of MnO_2 on them, changing the binding force between them could potentially improve the performance. Due to the larger electronegativity difference of 1.89 between oxygen and manganese as compared to the difference between carbon and manganese (1.00), substrate oxidation can be used to optimize the structure [82]. Direct comparison of $\text{MnO}_2/\text{g-CNFs-PRI}$ electrode and other substrate-oxidized ternary electrodes were made. Comparison between $\text{MnO}_2/\text{CNFs-PRI}$ and $\text{MnO}_2/\text{CNFs-1}$ electrodes are presented in Supplementary Information.

Fig. 7. Modification of the electrode materials by mild oxidation of reactive edges of vertical graphenes creates intricate hierarchical microstructure. FE-SEM images of (a) $\text{MnO}_2/\text{g-CNFs-1}$, (b) $\text{MnO}_2/\text{g-CNFs-3}$, (c) $\text{MnO}_2/\text{g-CNFs-5}$, and cross sections of (d) $\text{MnO}_2/\text{g-CNFs-1}$, (e) $\text{MnO}_2/\text{g-CNFs-3}$, (f) $\text{MnO}_2/\text{g-CNFs-5}$ samples. Notation of samples is explained in Table 1.

The inner fibers become more hydrophilic as more oxygen-containing functional groups were introduced, helping MnO_2 nanoparticles anchor on deep fiber network, shown in Fig. 7a-c. The nanosheets on g-CNFs-1 in the inset of Fig. 7a are thinner and more homogeneous than MnO_2 on other supports due to the lowest average thickness of 13.9 nm and SD value of 3.79 nm (Fig. S1). However, MnO_2 grew into non-uniform and thicker nanosheets on g-CNFs-3 (38.7 nm, Fig. S1) and then formed smaller clusters on g-CNFs-5, shown in the insets of Fig. 7b-c. Although the larger electronegativity difference between the edges and Mn^{2+} can reduce the nucleation energy and thus can decrease the number of atoms per nuclei, the oxidation degree of graphene walls also has an influence. Excessive oxygen-containing functional groups can destroy the sp^2 -hybridized orbits of graphene walls and weaken the electron concentration on edges, which impede the attachment and conversion of Mn^{2+} . As can be seen from Fig. 7d-f, MnO_2 anchor on edges without nanoparticles trapped in pores of VGs. The C, O, and Mn elements of $\text{MnO}_2/\text{g-CNFs-1}$ exhibited by SEM-EDX (energy dispersive X-ray) mapping further show the hierarchical structure (Fig. S7). The lack of Mn and O elements on fiber surface along the central position (Fig. S7a) and on bottom left of the cross section (Fig. S7b) support the combined effect on capacitance from both MnO_2 and VGs.

Fig. 8. Effects of mild oxidation on microstructure of hierarchical electrode materials. Raman spectra of (a) g-CNFs-PRI,

g-CNFs-1, g-CNFs-3, g-CNFs-5, and (b) the corresponding ternary composite electrodes; XPS spectra of (c) g-CNFs-PRI, g-CNFs-1, g-CNFs-3, g-CNFs-5, and (d) the corresponding composite electrodes.

Based on the Raman spectra in Fig. 8a, the I_D/I_G ratios of g-CNFs-1, g-CNFs-3, and g-CNFs-5 are 1.80, 1.72, and 1.86, respectively, notably lower compared to g-CNFs-PRI samples (2.38). The functionalization of both original edge defects and graphene walls are likely responsible for this variation. When oxidation was mild, filling of the edge-concentrated vacancy defects reduced the possibility of distortion of sp^2 orbitals on graphene walls, thereby decreasing the I_D/I_G ratio from 2.38 to 1.72. However, when oxidation time extended to 5 mins, more carbonyl groups formed on vertical graphene walls, leading to higher I_D/I_G ratio.

The deposition of MnO_2 diminished the D and G bands and made MnO_2 bands appeared in Fig. 8b, which show a reduced tendency as the prolonged oxidation time. The ratio of intensity of MnO_2 band (labeled as P) and the sum of I_D and I_G ($P/(I_D+I_G)$) is defined to quantify the substrate coverage by MnO_2 [83]. $P/(I_D+I_G)$ ratios for MnO_2 /g-CNFs-PRI, MnO_2 /g-CNFs-1, MnO_2 /g-CNFs-3, and MnO_2 /g-CNFs-5 are 0.37, 1.75, 1.40, and 0.25, respectively, corresponding to the SEM images in Fig. 2e and Fig. 6a-b.

Based on the XPS spectra in Fig. 8c, the C/O ratios of g-CNFs-1, g-CNFs-3, and g-CNFs-5 (17.17, 1.92, 1.73, and 1.46), together with the XPS de-convoluted C 1s spectra (Fig. S8) demonstrate the increase of oxygen-containing group content with the extension of oxidation time. The decrease of carbon contents is mainly produced by oxidation of C-C bond for g-CNFs-1 and then produced by oxidation of C=C bond for g-CNFs-3 and g-CNFs-5 (Fig. S8), which means that the binding sites for oxygen transferred from the defects on edges to the graphene walls with the oxidation time prolonged, resulting in the conductivity decrease. Peaks appearing in XPS spectra at about 80 and 650 eV in Fig. 8d herald successful MnO_2 -deposition. The manganese valence in MnO_2 on g-CNFs-1 support is 3.82 (Fig. S9), close to the Mn valence on g-CNFs-PRI support, suggesting 1-min oxidation hardly affecting the electrodeposition process. However, the manganese valences of MnO_2 /g-CNFs-3 (3.80) and MnO_2 /g-CNFs-5 (3.71) exhibit an opposite trend to C/O ratios, together with the morphologies in Fig. 7, proving excessive oxidation negatively affects the growth of MnO_2 .

C_M , C_A and C_V values in Fig. 9a-b and Fig. S10 are based on CV curves at scan rates from 2 to 200 $mV s^{-1}$ in three-electrode system (Fig. S3). The C_M (C_A , C_V) values at a scan rate of 2 $mV s^{-1}$ for MnO_2 /g-CNFs-PRI, MnO_2 /g-CNFs-1, MnO_2 /g-CNFs-3, and MnO_2 /g-CNFs-5 electrodes are 356 (48.9 $mF cm^{-2}$, 26.1 $F cm^{-3}$), 612 (61.2 $mF cm^{-2}$, 32.7 $F cm^{-3}$), 278 (48.6 $mF cm^{-2}$, 25.9 $F cm^{-3}$), and 256 $F g^{-1}$ (44.9 $mF cm^{-2}$, 23.9 $F cm^{-3}$), respectively. The enhanced hydrophilicity of the supports deliver enhanced EDLC than pristine ones, despite a lower drop for g-CNFs-5 due to the poor conductivity

(Fig. S10). As a result, the pure pseudocapacitive contributions of MnO_2 are 329, 521, 162, and 182 F g^{-1} (92%, 85%, 58%, and 71% in the total amount), respectively. The relationship between the mass loading and the contribution of pseudocapacitance of MnO_2 was also explored (Fig. S10). Considering the same electrode area, the C_A values also represent the total capacitances of the electrodes. The highest C_A value of $\text{MnO}_2/\text{g-CNFs-1}$ also reflects the structure superiority with relatively integrated graphene walls for good conductivity and refined MnO_2 nanosheets for sufficient contact with the electrolyte. The rate capabilities for the four electrodes at scan rate of 200 mV s^{-1} are 55.6%, 51.3%, 45.6%, and 36.5%, respectively. Compared with $\text{MnO}_2/\text{CNFs-PRI}$ electrode, the rate capability drop of $\text{MnO}_2/\text{g-CNFs-1}$ is not very obvious. The GCD result (Fig. S5) of $\text{MnO}_2/\text{g-CNFs-1}$ also shows the highest C_M value of 790 F g^{-1} at the scan rate of 2 A g^{-1} and a high rate capacity of 60% at the scan rate of 50 A g^{-1} (474 F g^{-1}). The CV advantages of $\text{MnO}_2/\text{g-CNFs-1}$ electrode are mainly ascribed to the moderate oxidation to the graphene walls, which supports good transfer of charge, smaller nanostructures, and improved EDLC effects. However, the excessively O-doped graphene walls and the MnO_2 arranged into larger thickness stacks or irregular nanoclusters of $\text{MnO}_2/\text{g-CNFs-3}$ and $\text{MnO}_2/\text{g-CNFs-5}$ restricted electron transport, decreased ion diffusion accesses to MnO_2 and VGs, and lowered the material utilization efficiency, resulting in inferior CV performance.

Fig. 9. Mild oxidation further improves the high-frequency response, energy and specific power of the hierarchical hybrid electrodes. (a-b) C_M and C_A values vs. scan rate, (c) capacitance retention after a cycle stability test, and (d) Nyquist plots (line represents fitting data, and scatter raw data) for $\text{MnO}_2/\text{g-CNFs-PRI}$, $\text{MnO}_2/\text{g-CNFs-1}$, $\text{MnO}_2/\text{g-CNFs-3}$, and $\text{MnO}_2/\text{g-CNFs-5}$ in a three-electrode system; (e) the real and imaginary parts of the capacitance vs. frequency based on the EIS tests; (f) CV curves at different scan rates at a potential window of 2 V, (g) GCD curves at different scan rates at a potential window of 2 V, (h) Capacitance retention after 5000 CV cycles at the scan rate of 100 mV s^{-1} at the potential window of 2V, and (i) Ragone plot for AMG.

The specific capacitance retention for $\text{MnO}_2/\text{g-CNFs-1}$, $\text{MnO}_2/\text{g-CNFs-3}$, and $\text{MnO}_2/\text{g-CNFs-5}$ electrodes after 5000 CV cycles at the scan rate of 100 mV s^{-1} are 109%, 106%, and 105%, respectively (Fig. 9c), much higher than $\text{MnO}_2/\text{g-CNFs-PRI}$ samples (93%). Undoubtedly, tight adhesion between the oxidized substrates and nanostructured MnO_2 helped alleviate the stability problem [75, 76]. The capacitance retention exceeding 100% can be due to the activation of MnO_2 nanosheets by progressive penetration of electrolyte [84, 85]. The declining trend may be related to the imperfections in dispersion and size of MnO_2 nanostructures. Indeed, the more dispersive and smaller MnO_2

nanostructures present, the smaller internal space is for electrolytes penetration during the cycling performance tests. Compared with other MnO_2 -based composite electrode reported before, $\text{MnO}_2/\text{g-CNFs-1}$ exhibits comparable C_M , C_A , and C_V values [39, 86], and other electrochemical performance (Table S1). The R_s values of $\text{MnO}_2/\text{g-CNFs-PRI}$, $\text{MnO}_2/\text{g-CNFs-1}$, $\text{MnO}_2/\text{g-CNFs-3}$, and $\text{MnO}_2/\text{g-CNFs-5}$ electrodes in Fig. 9d are 5.6, 4.3, 4.7, and 4.9 Ω , respectively. The highest R_s value of $\text{MnO}_2/\text{g-CNFs-PRI}$ confirms the importance of the electrode hydrophilicity. The other values evidence the inverse relation between the conductivity and the oxidation degree. R_{ct} values of $\text{MnO}_2/\text{g-CNFs-1}$ is 5.3 Ω , smaller than $\text{MnO}_2/\text{g-CNFs-PRI}$ (7.1 Ω), $\text{MnO}_2/\text{g-CNFs-3}$ (6.1 Ω), and $\text{MnO}_2/\text{g-CNFs-5}$ (9.7 Ω) samples, seen from the magnified plots in Fig. 9d. Compared with the other three electrodes, the smaller size of nanosheets on g-CNFs-1 and the relative integrity of graphene walls promote charge accumulation at MnO_2 surfaces, reducing the ion (N^+) transfer resistance from the electrolyte to the electrode. The customized MnO_2 nanostructures on g-CNFs-1 together with the numerous pores among the structures ensure low ion diffusion resistance, thereby reducing the projection of the Warburg region and increasing the slope of the tail. The $C(\omega)$ values of $\text{MnO}_2/\text{g-CNFs-PRI}$ and $\text{MnO}_2/\text{g-CNFs-1}$ at 0.01 Hz in Fig. 9e are still consistent with the CV results. The slightly longer CRCTC of $\text{MnO}_2/\text{g-CNFs-1}$ (3.2 s) than that of $\text{MnO}_2/\text{g-CNFs-PRI}$ (1.5 s) further demonstrates the slightly oxidation-reduced conductivity. Double layer capacitances (C_{dl}) were further tested to evaluate the specific surface area of these electrodes by CV curves based on $I_A = sC_{dl}$, where s is the scan rate, and C_{dl} is the slope of I vs. s curves [87, 88]. I is the areal current density (geometrical area of the electrodes), calculated by half of the difference of the current density during the forward and reverse sweeps. The CV tests were collected at up and down 0.2 V of the balanced voltage (0.58 ± 0.02 V) in a three-electrode system (Fig. S11). The C_{dl} values of $\text{MnO}_2/\text{CNFs-PRI}$, $\text{MnO}_2/\text{CNFs-1}$, $\text{MnO}_2/\text{g-CNFs-PRI}$, $\text{MnO}_2/\text{g-CNFs-1}$, $\text{MnO}_2/\text{g-CNFs-3}$, and $\text{MnO}_2/\text{g-CNFs-5}$ are 5.55, 5.75, 6.54, 9.54, 7.57, 5.98 mF cm^{-2} , respectively. The highest C_{dl} value of $\text{MnO}_2/\text{g-CNFs-1}$ suggests a higher specific surface area than other electrodes, corresponding to the good hierarchical structure and the electrochemical performance.

As for AMG with matched electrode masses ($\text{MnO}_2/\text{g-CNFs-1}$: g-CNFs-PRI = 0.18) according to Fig. S12, the associated CV and GCD curves in Fig. S12 are of a similar shape despite the window potential, indicating good capacitive performance. They are still in a good shape even at high scan rates at the potential window of 2 V in Fig. 9f, exhibiting ideal capacitive performance. The GCD curve of AMG at scan rate of 1 A g^{-1} at the potential window of 2 V in Fig. 9g reaches a comparable C_M value (Fig. S12b-c) of 128 F g^{-1} (3.79 F cm^{-3} , based on the volume of both electrode) with previous reports [68, 89]. AMG also shows a specific capacitance drop of less than 5% after 5000 CV cycles at 100 mV s^{-1} at the potential window of 2V, shown in Fig. 9h, suggesting a relatively stable electrode structure even under the

high potential. Due to the wide potential window, the AMG device displays a specific energy of 30.4 Wh kg^{-1} (0.90 mWh cm^{-3}) and a specific power of 27.8 kW kg^{-1} (824 mW cm^{-3}) at a scan rate of 15 A g^{-1} in Fig. 9i, which is competitive with other reported studies [90-99].

4. Conclusion

A novel hierarchical nanocarbon-MnO₂ structure is fabricated for combining the pseudocapacitance of MnO₂ and EDLC of nanocarbon materials. MnO₂ grows into thin and uniform nanosheets on mildly oxidized edges of VGs, which fully expose the graphene walls to electrolyte ions. The improved reactivity of the MnO₂ nanostructures and the remarkable intrinsic advantages of the exposed VGs made the hierarchical hybrid electrode exhibit high specific capacitance, good rate capability, excellent cycle stability, low resistance in three-electrode system. The asymmetric electrode system of the hierarchical hybrid electrode and g-CNFs-PRI shows excellent values of the specific energy and specific power. Besides, benefiting from the electrospinning CNFs support, the electrode maintained ideal mechanical property even after a long cycle stability test. This work opens new opportunities for the development of advanced hierarchical nanostructured electrode materials which combine the maximized benefits of electrostatic double layer and pseudocapacitive charge storage mechanisms.

Data availability

The raw/processed data required to reproduce these findings cannot be shared at this time as the data also forms part of an ongoing study.

References

- [1] A. S. Arico, P. Bruce, B. Scrosati, J. M. Tarascon and W. Van Schalkwijk, *Nat. Mater.* 4 (2005) 366-377.
- [2] P. Simon and Y. Gogotsi, *Nat. Mater.* 7 (2008) 845-854.
- [3] F. Bonaccorso, L. Colombo, G. H. Yu, M. Stoller, V. Tozzini, A. C. Ferrari, R. S. Ruoff and V. Pellegrini, *Science* 347 (2015).
- [4] C. Liu, F. Li, L. P. Ma and H. M. Cheng, *Adv. Mater.* 22 (2010) E28-E62.
- [5] J. Yan, Q. Wang, T. Wei and Z. J. Fan, *Adv. Energy Mater.* 4 (2014).
- [6] Z. N. Yu, L. Tetard, L. Zhai and J. Thomas, *Energy Environ. Sci.* 8 (2015) 702-730.
- [7] B. E. Conway, *J. Electrochem. Soc.* 138 (1991) 1539-1548.
- [8] B. Conway and W. Pell, *J. Solid State Electrochem.* 7 (2003) 637-644.
- [9] Z. S. Wu, X. L. Feng and H. M. Cheng, *Natl. Sci. Rev.* 1 (2014) 277-292.
- [10] A. G. Pandolfo and A. F. Hollenkamp, *J. Power Sources* 157 (2006) 11-27.
- [11] P. Kleszyk, P. Ratajczak, P. Skowron, J. Jagiello, Q. Abbas, E. Frackowiak and F. Beguin, *Carbon* 81 (2015) 148-157.
- [12] Y. B. Tan and J. M. Lee, *J. Mater. Chem. A* 1 (2013) 14814-14843.
- [13] W. Lv, Z. J. Li, Y. Q. Deng, Q. H. Yang and F. Y. Kang, *Energy Storage Mater.* 2 (2016) 107-138.
- [14] D. P. Dubal, O. Ayyad, V. Ruiz and P. Gomez-Romero, *Chem. Soc. Rev.* 44 (2015) 1777-1790.

- [15] Y. G. Wang, Y. F. Song and Y. Y. Xia, *Chem. Soc. Rev.* 45 (2016) 5925-5950.
- [16] I. E. Rauda, V. Augustyn, B. Dunn and S. H. Tolbert, *Acc. Chem. Res.* 46 (2013) 1113-1124.
- [17] V. Augustyn, P. Simon and B. Dunn, *Energy Environ. Sci.* (2014) Medium: X; Size: 1597-1614.
- [18] Y. F. Zhang, L. Q. Li, H. Q. Su, W. Huang and X. C. Dong, *J. Mater. Chem. A* 3 (2015) 43-59.
- [19] H. Y. Li, K. Jiao, L. Wang, C. Wei, X. L. Li and B. Xie, *J. Mater. Chem. A* 2 (2014) 18806-18815.
- [20] G. H. Cheng, W. F. Yang, C. Q. Dong, T. Y. Kou, Q. G. Bai, H. Wang and Z. H. Zhang, *J. Mater. Chem. A* 3 (2015) 17469-17478.
- [21] Y. G. Guo, J. S. Hu and L. J. Wan, *Adv. Mater.* 20 (2008) 2878-2887.
- [22] L. Z. Fan, Y. S. Hu, J. Maier, P. Adelhelm, B. Smarsly and M. Antonietti, *Adv. Funct. Mater.* 17 (2007) 3083-3087.
- [23] W. M. Zhang, J. S. Hu, Y. G. Guo, S. F. Zheng, L. S. Zhong, W. G. Song and L. J. Wan, *Adv. Mater.* 20 (2008) 1160-1165.
- [24] J. J. Xu, K. Wang, S. Z. Zu, B. H. Han and Z. X. Wei, *ACS Nano* 4 (2010) 5019-5026.
- [25] C. Z. Yuan, X. G. Zhang, L. H. Su, B. Gao and L. F. Shen, *J. Mater. Chem.* 19 (2009) 5772-5777.
- [26] M. Huang, F. Li, F. Dong, Y. X. Zhang and L. L. Zhang, *J. Mater. Chem. A* 3 (2015) 21380-21423.
- [27] Y. Ando, X. Zhao and M. Ohkohchi, *Carbon* 35 (1997) 153-158.
- [28] Y. H. Wang, Y. S. Liu and I. Zhitomirsky, *J. Mater. Chem. A* 1 (2013) 12519-12526.
- [29] M. A. Cheney, S. W. Joo, A. Banerjee and B. K. Min, *J. Colloid Interface Sci.* 379 (2012) 141-143.
- [30] G. H. Yu, X. Xie, L. J. Pan, Z. N. Bao and Y. Cui, *Nano Energy* 2 (2013) 213-234.
- [31] H. Y. Wang, C. M. Xu, Y. Q. Chen and Y. Wang, *Energy Storage Mater.* 8 (2017) 127-133.
- [32] K. M. Energy & Environmental ScienceActa CrystallographicaParida, S. B. Kanungo and B. R. Sant, *Electrochim. Acta* 26 (1981) 435-443.
- [33] M. Toupin, T. Brousse and D. Belanger, *Chem. Mater.* 16 (2004) 3184-3190.
- [34] M. Xu, L. Kong, W. Zhou and H. Li, *J. Phys. Chem. C* 111 (2007) 19141-19147.
- [35] W. F. Wei, X. W. Cui, W. X. Chen and D. G. Ivey, *Chem. Soc. Rev.* 40 (2011) 1697-1721.
- [36] G. Han, Y. Liu, L. Zhang, E. Kan, S. Zhang, J. Tang and W. Tang, *Sci. Rep.* 4 (2014) 4824.
- [37] J. Chang, M. Jin, F. Yao, T. H. Kim, V. T. Le, H. Yue, F. Gunes, B. Li, A. Ghosh, S. Xie and Y. H. Lee, *Adv. Funct. Mater.* 23 (2013) 5074-5083.
- [38] Y. Hou, Y. W. Cheng, T. Hobson and J. Liu, *Nano Lett.* 10 (2010) 2727-2733.
- [39] Z. Y. Zhang, F. Xiao, J. Xiao and S. Wang, *J. Mater. Chem. A* 3 (2015) 11817-11823.
- [40] C. Z. Yang, M. Zhou and Q. Xu, *Phys. Chem. Chem. Phys.* 15 (2013) 19730-19740.
- [41] Y. Wang, Z. J. Han, S. F. Yu, R. R. Song, H. H. Song, K. Ostrikov and H. Y. Yang, *Carbon* 64 (2013) 230-236.
- [42] B. Conway and E. Gileadi, *Trans. Faraday Society* 58 (1962) 2493-2509.
- [43] Z. Chen, Y. C. Qin, D. Weng, Q. F. Xiao, Y. T. Peng, X. L. Wang, H. X. Li, F. Wei and Y. F. Lu, *Adv. Funct. Mater.* 19 (2009) 3420-3426.
- [44] H. Zhang, G. P. Cao, Z. Y. Wang, Y. S. Yang, Z. J. Shi and Z. N. Gu, *Nano Lett.* 8 (2008) 2664-2668.
- [45] Z. Bo, S. Mao, Z. J. Han, K. F. Cen, J. H. Chen and K. Ostrikov, *Chem. Soc. Rev.* 44 (2015) 2108-2121.
- [46] S. Mao, K. H. Yu, J. B. Chang, D. A. Steeber, L. E. Ocola and J. H. Chen, *Sci. Rep.* 3 (2013).
- [47] L. N. Dong, X. J. Quan and P. Cheng, *Int. J. Heat Mass Transfer* 55 (2012) 4376-4384.
- [48] J. Zhao, M. Shaygan, J. Eckert, M. Meyyappan and M. H. Rummeli, *Nano Lett.* 14 (2014) 3064-3071.
- [49] J. P. Randin and E. Yeager, *J. Electrochem. Soc.* 118 (1971) 711-714.
- [50] W. J. Yuan, Y. Zhou, Y. R. Li, C. Li, H. L. Peng, J. Zhang, Z. F. Liu, L. M. Dai and G. Q. Shi, *Sci. Rep.* 3 (2013).
- [51] H. C. Yang, J. Y. Yang, Z. Bo, S. Zhang, J. H. Yan and K. F. Cen, *J. Power Sources* 324 (2016) 309-316.
- [52] H. C. Yang, X. L. Zhang, J. Y. Yang, Z. Bo, M. Hu, J. H. Yan and K. F. Cen, *J. Phys. Chem. Lett.* 8 (2017) 153-160.
- [53] K. H. Yu, G. H. Lu, Z. Bo, S. Mao and J. H. Chen, *J. Phys. Chem. Lett.* 2 (2011) 1556-1562.
- [54] S. L. Zhai, H. E. Karahan, L. Wei, Q. H. Qian, A. T. Harris, A. I. Minett, S. Ramakrishna, A. K. Ng and Y. Chen, *Energy Storage Mater.* 3 (2016) 123-139.
- [55] D. H. Reneker and I. Chun, *Nanotechnology* 7 (1996) 216-223.

- [56] B. A. Zhang, F. Y. Kang, J. M. Tarascon and J. K. Kim, *Prog. Mater. Sci.* 76 (2016) 319-380.
- [57] Z. Y. Wang and Z. H. Dai, *Nanoscale* 7 (2015) 6420-6431.
- [58] S. J. He and W. Chen, *J. Power Sources* 294 (2015) 150-158.
- [59] P. Lv, P. Zhang, Y. Y. Feng, Y. Li and W. Feng, *Electrochim. Acta* 78 (2012) 515-523.
- [60] Y. W. Chen, L. L. Chen, P. W. Li, Y. Xu, M. J. Fan, S. M. Zhu and S. B. Shen, *Energy* 109 (2016) 620-628.
- [61] L. W. Ji, A. J. Medford and X. W. Zhang, *J. Mater. Chem.* 19 (2009) 5593-5601.
- [62] P. Zhang, M. He, S. Xu and X. B. Yan, *J. Mater. Chem. A* 3 (2015) 10811-10818.
- [63] Y. M. He, W. J. Chen, C. T. Gao, J. Y. Zhou, X. D. Li and E. Q. Xie, *Nanoscale* 5 (2013) 8799-8820.
- [64] J. H. Kim, K. H. Lee, L. J. Overzet and G. S. Lee, *Nano Lett.* 11 (2011) 2611-2617.
- [65] S. Komaba, T. Tsuchikawa, M. Tomita, N. Yabuuchi and A. Ogata, *J. Electrochem. Soc.* 160 (2013) A1952-A1961.
- [66] W. Wei, X. B. Huang, Y. M. Tao, K. Y. Chen and X. Z. Tang, *Phys. Chem. Chem. Phys.* 14 (2012) 5966-5972.
- [67] Z. M. Hu, X. Xiao, C. Chen, T. Q. Li, L. Huang, C. F. Zhang, J. Su, L. Miao, J. J. Jiang, Y. R. Zhang and J. Zhou, *Nano Energy* 11 (2015) 226-234.
- [68] Y. C. Liu, X. F. Miao, J. H. Fang, X. X. Zhang, S. J. Chen, W. Li, W. D. Feng, Y. Q. Chen, W. Wang and Y. N. Zhang, *ACS Appl. Mater. Interfaces* 8 (2016) 5251-5260.
- [69] S. Razoumov, A. Klementov, S. Litvinenko and A. Beliaikov, *US* 6222723, 2001.
- [70] L. S. Zhang, Y. P. Huang, Y. F. Zhang, H. H. Gu, W. Fan and T. X. Liu, *Adv. Mater. Interfaces* 3 (2016).
- [71] S. Bag and C. R. Raj, *J. Mater. Chem. A* 4 (2016) 587-595.
- [72] A. Benayad, H. J. Shin, H. K. Park, S. M. Yoon, K. K. Kim, M. H. Jin, H. K. Jeong, J. C. Lee, J. Y. Choi and Y. H. Lee, *Chem. Phys. Lett.* 475 (2009) 91-95.
- [73] X. Zhao, Y. X. Du, Y. Z. Li and Q. H. Zhang, *Ceram. Int.* 41 (2015) 7402-7410.
- [74] H. M. Zhu, Q. Liu, J. Y. Liu, R. M. Li, H. S. Zhang, S. X. Hu and Z. S. Li, *Electrochim. Acta* 178 (2015) 758-766.
- [75] W. F. Wei, X. W. Cui, W. X. Chen and D. G. Ivey, *J. Power Sources* 186 (2009) 543-550.
- [76] Z. J. Han, D. H. Seo, S. Yick, J. H. Chen and K. Ostrikov, *Npg Asia Mater.* 6 (2014).
- [77] S. Löffler and A. Richter-Dahlfors, *J. Mater. Chem. B* 3 (2015) 4997-5000.
- [78] G. Q. Tan, F. Wu, L. Li, R. J. Chen and S. Chen, *J. Phys. Chem. C* 117 (2013) 6013-6021.
- [79] X. H. Wang, Y. H. Li, F. L. Lou, M. E. M. Buan, E. Sheridan and D. Chen, *Rsc Adv.* 7 (2017) 23859-23865.
- [80] V. Ganesh, S. Pitchumani and V. Lakshminarayanan, *J. Power Sources* 158 (2006) 1523-1532.
- [81] G. P. Xiong, K. P. S. S. Hembram, R. G. Reifemberger and T. S. Fisher, *J. Power Sources* 227 (2013) 254-259.
- [82] M. Kim, Y. Hwang, K. Min and J. Kim, *Electrochim. Acta* 113 (2013) 322-331.
- [83] S. Chen, J. W. Zhu, X. D. Wu, Q. F. Han and X. Wang, *ACS Nano* 4 (2010) 2822-2830.
- [84] J. Menzel, K. Fic, M. Meller and E. Frackowiak, *J. Appl. Electrochem.* 44 (2014) 439-445.
- [85] Y. C. Zhao, S. Li and C. A. Wang, *Ecs J. Solid State Sc.* 5 (2016) M5-M11.
- [86] L. Lim, Y. S. Liu, W. W. Liu, R. Tjandra, L. Rasenthiram, Z. W. Chen and A. P. Yu, *ACS Appl. Mater. Interfaces* 9 (2017) 39576-39583.
- [87] M. W. Xie, L. Yang, Y. Y. Ji, Z. Q. Wang, X. Ren, Z. Liu, A. M. Asiri, X. L. Xiong and X. P. Sun, *Nanoscale* 9 (2017) 16612-16615.
- [88] M. J. Gira, K. P. Tkacz and J. R. Hampton, *Nano Converg* 3 (2016) 6.
- [89] P. Sun, H. Yi, T. Q. Peng, Y. T. Jing, R. J. Wang, H. W. Wang and X. F. Wang, *J. Power Sources* 341 (2017) 27-35.
- [90] D. Gueon and J. H. Moon, *ACS Sustain Chem. Eng.* 5 (2017) 2445-2453.
- [91] J. Y. Dong, G. Lu, F. Wu, C. X. Xu, X. H. Kang and Z. M. Cheng, *Appl. Surf. Sci.* 427 (2018) 986-993.
- [92] Z. B. Lei, J. T. Zhang and X. S. Zhao, *J. Mater. Chem.* 22 (2012) 153-160.
- [93] H. C. Gao, F. Xiao, C. B. Ching and H. W. Duan, *ACS Appl. Mater. Interfaces* 4 (2012) 2801-2810.
- [94] Z. N. Yu, B. Duong, D. Abbitt and J. Thomas, *Adv. Mater.* 25 (2013) 3302-3306.
- [95] H. Jiang, L. P. Yang, C. Z. Li, C. Y. Yan, P. S. Lee and J. Ma, *Energy Environ. Sci.* 4 (2011) 1813-1819.
- [96] Z. J. Fan, J. Yan, T. Wei, L. J. Zhi, G. Q. Ning, T. Y. Li and F. Wei, *Adv. Funct. Mater.* 21 (2011) 2366-2375.
- [97] P. C. Chen, G. Z. Shen, Y. Shi, H. T. Chen and C. W. Zhou, *ACS Nano* 4 (2010) 4403-4411.

[98] X. Zhao, L. L. Zhang, S. Murali, M. D. Stoller, Q. H. Zhang, Y. W. Zhu and R. S. Ruoff, ACS Nano 6 (2012) 5404-5412.

[99] Z. S. Wu, W. C. Ren, D. W. Wang, F. Li, B. L. Liu and H. M. Cheng, ACS Nano 4 (2010) 5835-5842.

Accepted manuscript

Table 1. Notation and performance of different composite electrodes

Samples	Supports	Oxidation time	Specific capacitance (2 mV s ⁻¹)	Specific energy (15 A g ⁻¹)	Capacitance retention (5000 CV cycles)
MnO ₂ /CNFs-PRI	CNFs	0	257 F g ⁻¹	/	88%
MnO ₂ /g-CNFs-PRI	VGs deposited on CNFs	0	356 F g ⁻¹	/	93%
MnO ₂ /CNFs-1	CNFs	1 min	444 F g ⁻¹	/	107%
MnO ₂ /g-CNFs-1	VGs deposited on CNFs	1 min	612 F g ⁻¹	/	109%
MnO ₂ /g-CNFs-3	VGs deposited on CNFs	3 min	278 F g ⁻¹	/	106%
MnO ₂ /g-CNFs-5	VGs deposited on CNFs	5 min	256 F g ⁻¹	/	105%
MnO ₂ /g-CNFs-1//g-CNFs-PRI	VGs deposited on CNFs	1 min	128 F g ⁻¹	30.4	95.5%

Figure captions

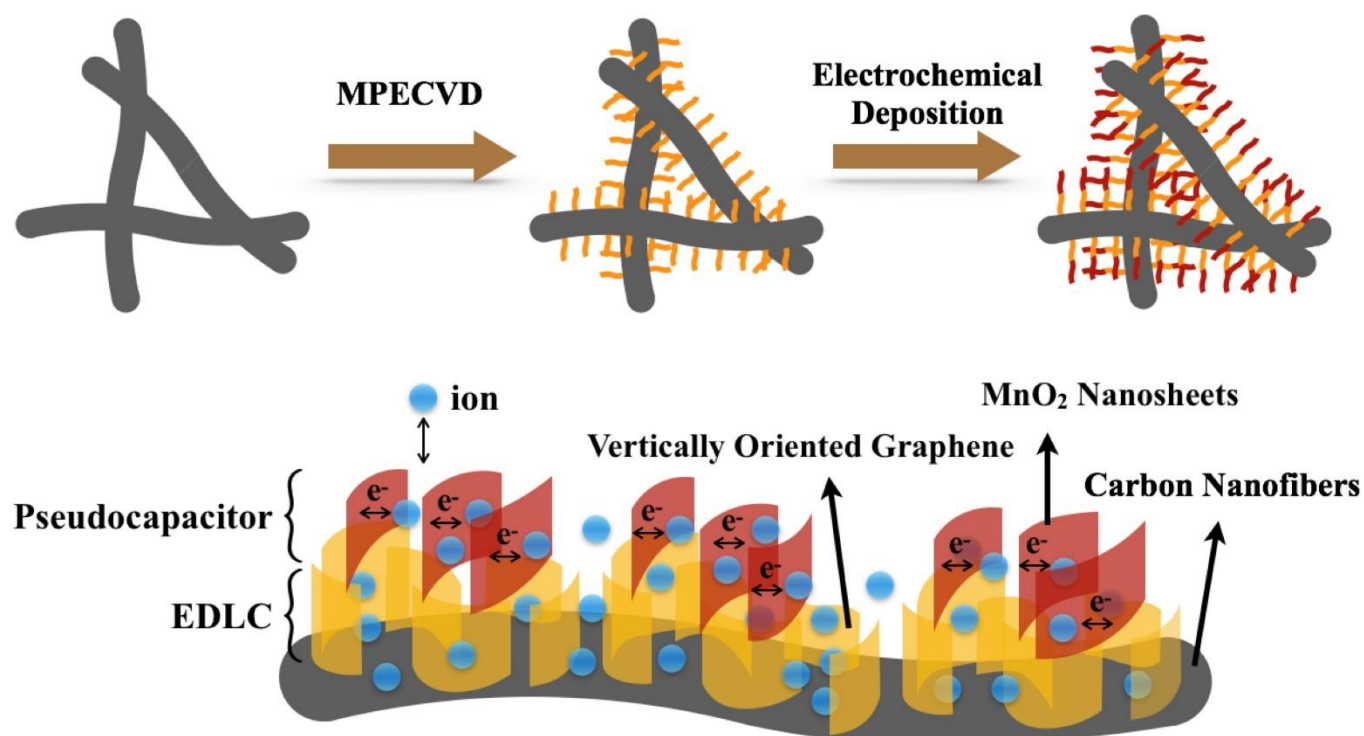


Fig. 1. Synergy of electrostatic double layer and pseudocapacitive effects realized by hierarchical stacking of MnO_2 on the edges of VGs supported by large-area, flexible carbon nanofibers. This way of stacking fully opens the side-walls of VGs to electrolyte ions and ensures maximum efficiency from both primary mechanisms of charge storage. High conductivity of VGs and CNFs and covalent bonding between them ensure high charge transfer rates leading to excellent specific energy and power of the nanostructured hierarchical hybrid electrochemical capacitor electrode.

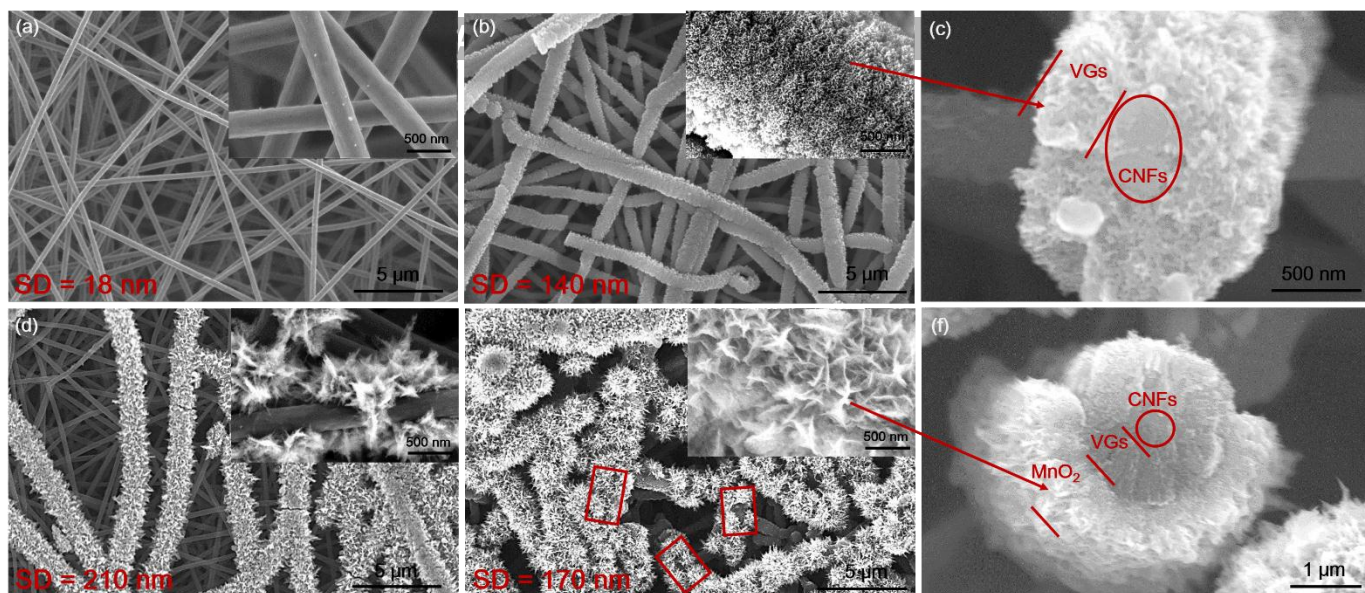


Fig. 2. Microstructure of the hierarchical hybrid electrodes imaged by FE-SEM shows the possibility to arrange MnO₂ nanosheets on top of the VGs edges, while the VGs are supported by carbon nanofibers. FE-SEM images of (a) CNFs, (b) g-CNFs, (c) Cross section of g-CNFs, (d) MnO₂/CNFs-PRI, (e) MnO₂/g-CNFs-PRI, and (f) Cross section of MnO₂/g-CNFs-PRI. Notation of samples is explained in Table 1.

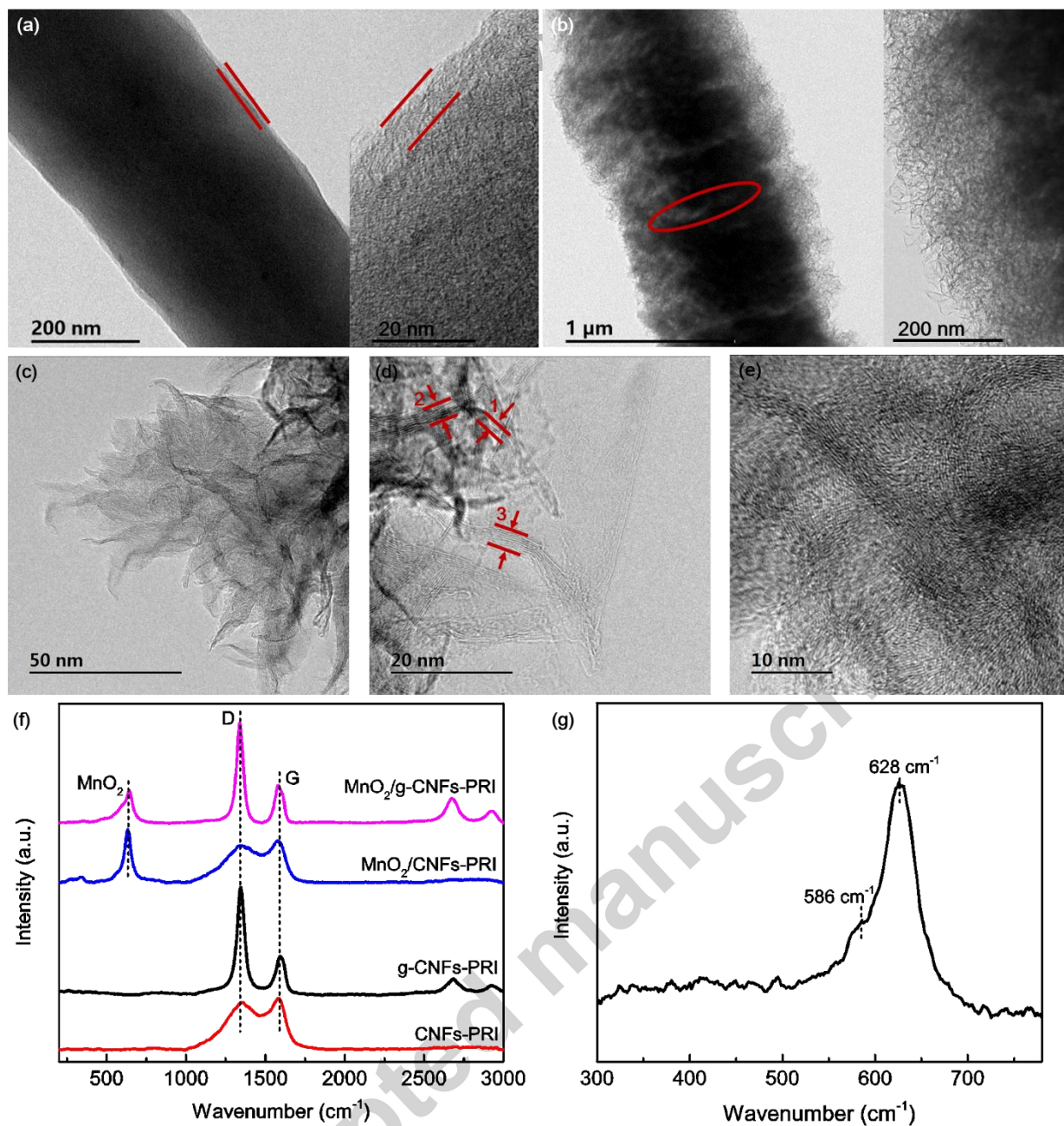


Fig. 3. Transmission electron microscopy showing dense patterns of VGs seamlessly incorporated into the supporting carbon nanofiber structure. TEM and magnified TEM images of (a) CNFs-PRI and (b) g-CNFs-PRI samples; TEM (c) and HRTEM (d-e) images of VGs; locations 1, 2, and 3 in (d) show VGs sheets with 3, 6, and 9 layers; (f) Raman spectra of the various electrode materials; (g) High resolution Raman spectrum of MnO₂/g-CNFs-PRI sample.

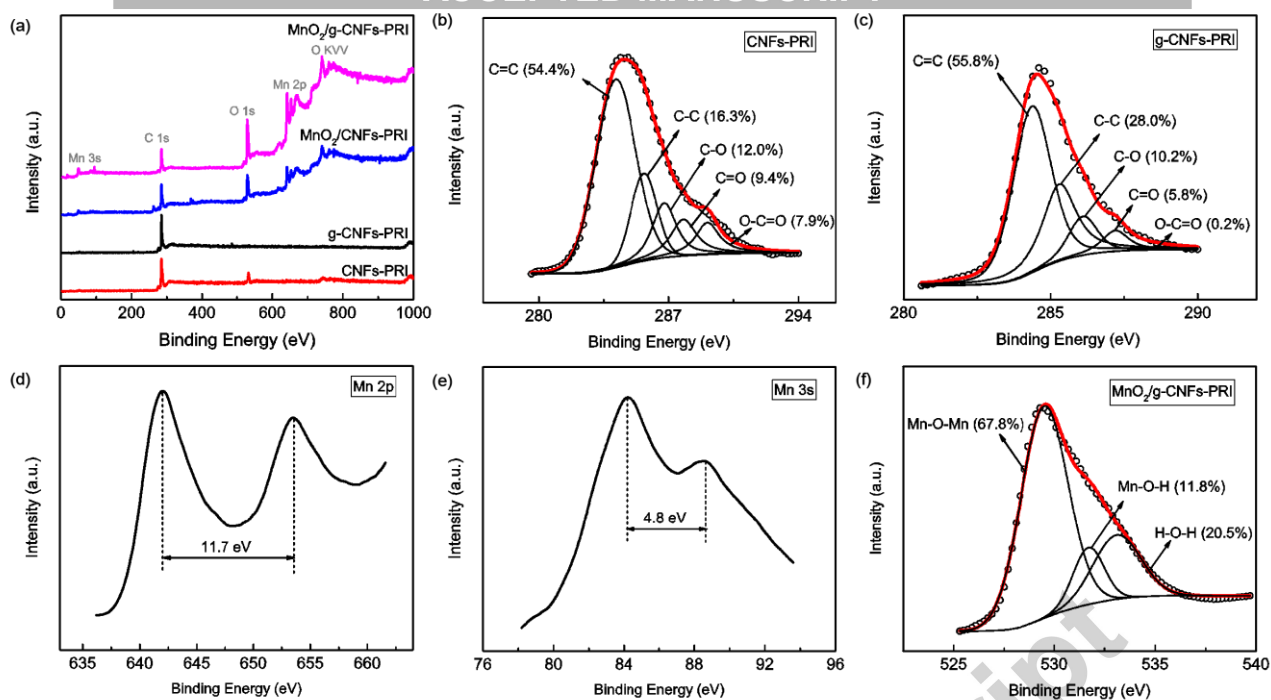


Fig. 4. XPS analysis reveals dominant carbon-carbon and Mn-oxygen bonds which are beneficial for both structural stability and dual charge storage mechanism. (a) XPS spectra of various electrode materials; Deconvoluted XPS C 1s spectra of (b) CNFs-PRI and (c) g-CNFs-PRI; (d) XPS Mn 2p, (e) Mn 3s, and (f) Deconvoluted O 1S spectrum of $\text{MnO}_2/\text{g-CNFs-PRI}$.

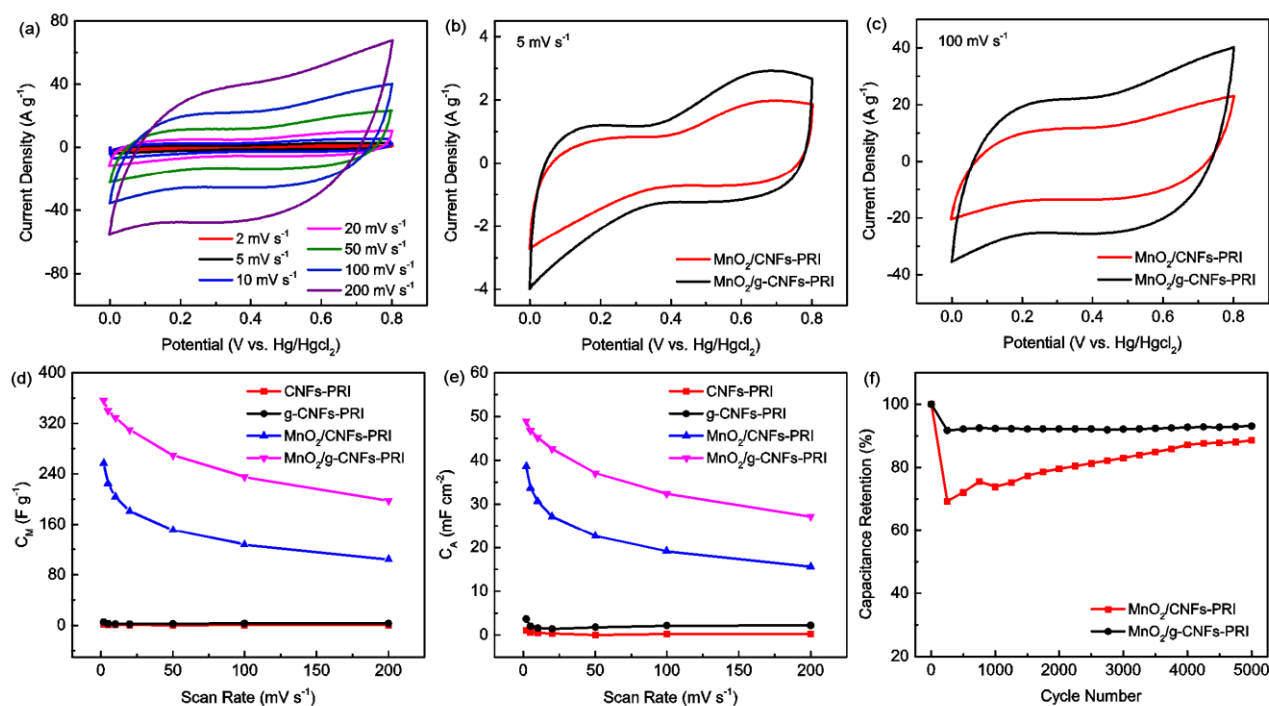


Fig. 5. Substantial improvement of electrochemical performance by stacking of MnO₂ nanosheets on top of VG edges in a three-electrode system. (a) The whole CV curves for MnO₂/g-CNFs-PRI; (b-c) CV curve comparisons for MnO₂/CNFs-PRI and MnO₂/g-CNFs-PRI at different scan rates; (d-e) C_M and C_A values vs. scan rate for various electrode materials; (f) Capacitance retention for MnO₂/CNFs-PRI and MnO₂/g-CNFs-PRI after a cycle stability test.

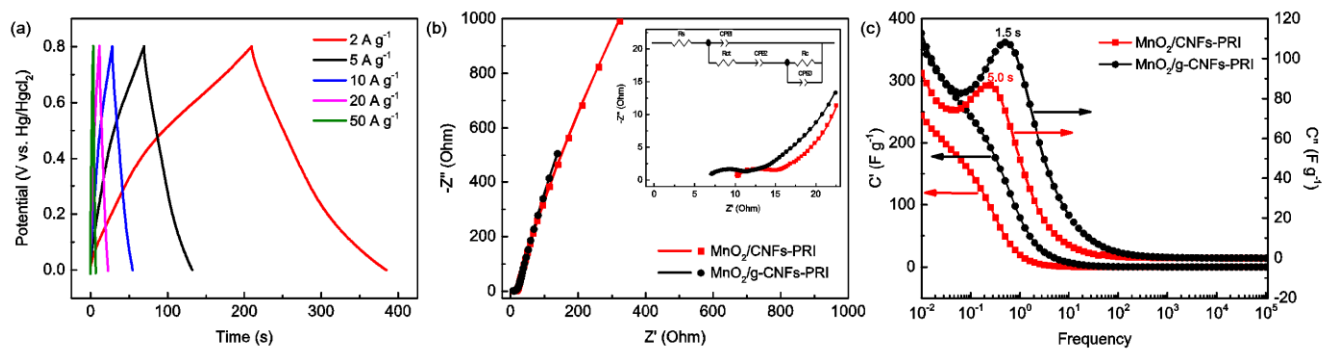


Fig. 6. Hybrid hierarchical electrodes show good high-frequency response in a three-electrode system. (a) The whole GCD curves for MnO₂/g-CNFs-PRI; (b) Nyquist plots (line represents fitting data, and scatter raw data) and equivalent circuit in the inset, and (c) the real and imaginary parts of capacitance vs. frequency for MnO₂/g-CNFs-PRI and MnO₂/CNFs-PRI samples.

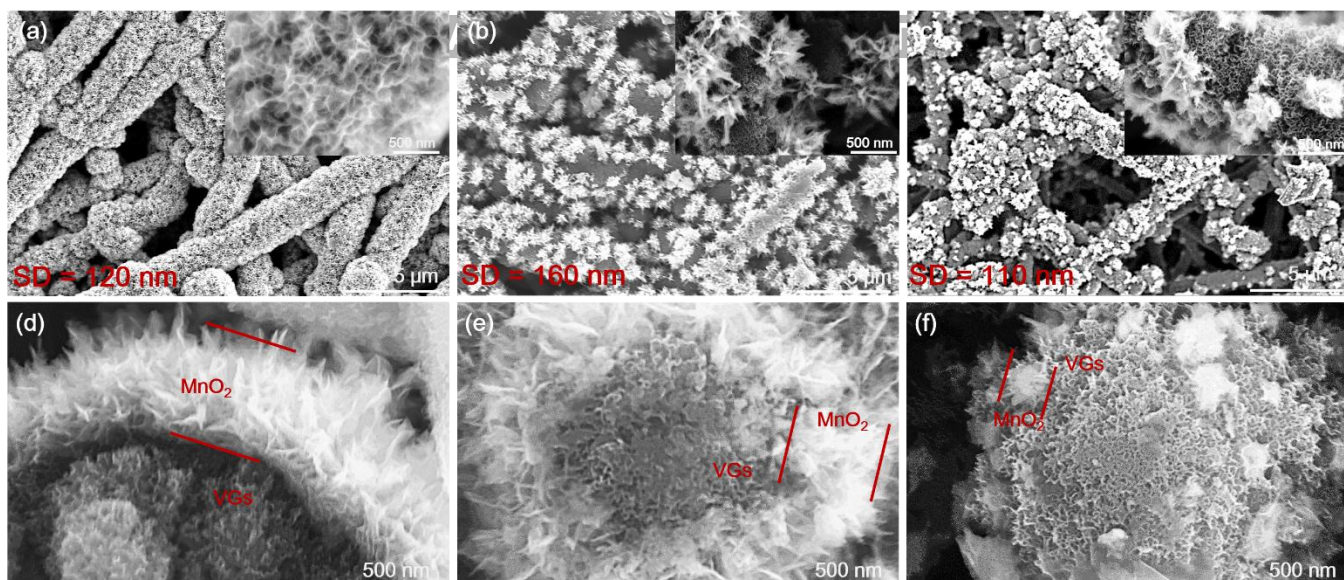


Fig. 7. Modification of the electrode materials by mild oxidation of reactive edges of vertical graphenes creates intricate hierarchical microstructure. FE-SEM images of (a) $\text{MnO}_2/\text{g-CNFs-1}$, (b) $\text{MnO}_2/\text{g-CNFs-3}$, (c) $\text{MnO}_2/\text{g-CNFs-5}$, and cross sections of (d) $\text{MnO}_2/\text{g-CNFs-1}$, (e) $\text{MnO}_2/\text{g-CNFs-3}$, (f) $\text{MnO}_2/\text{g-CNFs-5}$ samples. Notation of samples is explained in Table 1.

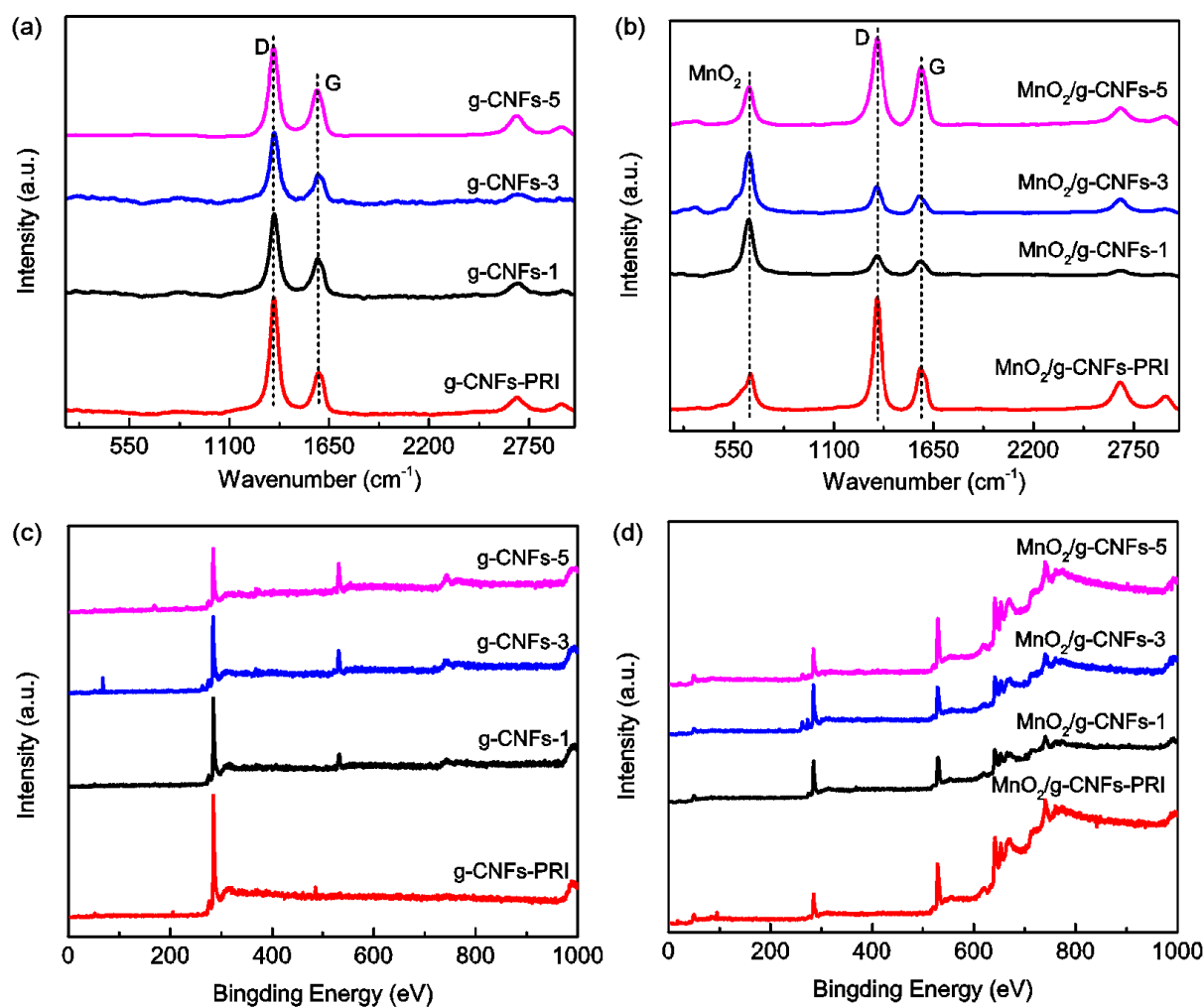


Fig. 8. Effects of mild oxidation on microstructure of hierarchical electrode materials. Raman spectra of (a) g-CNFs-PRI, g-CNFs-1, g-CNFs-3, g-CNFs-5, and (b) the corresponding ternary composite electrodes; XPS spectra of (c) g-CNFs-PRI, g-CNFs-1, g-CNFs-3, g-CNFs-5, and (d) the corresponding composite electrodes.

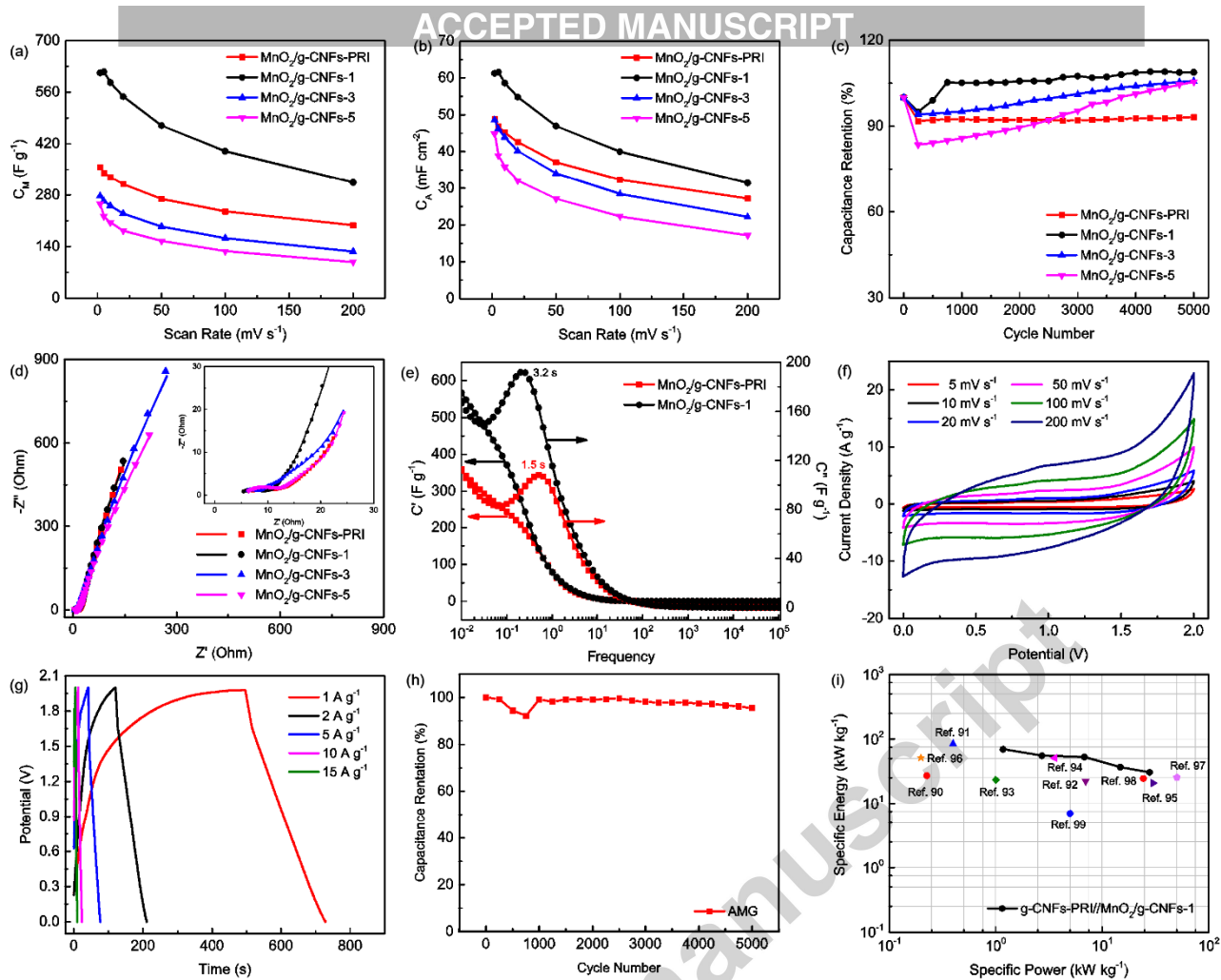


Fig. 9. Mild oxidation further improves the electrochemical performance of the hierarchical hybrid electrodes. (a-b) C_M and C_A values vs. scan rate, (c) capacitance retention after a cycle stability test, and (d) Nyquist plots (line represents fitting data, and scatter raw data) for MnO₂/g-CNFs-PRI, MnO₂/g-CNFs-1, MnO₂/g-CNFs-3, and MnO₂/g-CNFs-5 in a three-electrode system; (e) the real and imaginary parts of the capacitance vs. frequency based on the EIS tests; (f) CV curves at different scan rates at a potential window of 2 V, (g) GCD curves at different scan rates at a potential window of 2 V, (h) Capacitance retention after 5000 CV cycles at the scan rate of 100 mV s⁻¹ at the potential window of 2V, and (i) Ragone plot for AMG.